Journal of Engineering for Gas Turbines and Power

GTP-21-1139

SIMULATION OF A SIMPLIFIED AEROENGINE BEARING CHAMBER USING A FULLY COUPLED TWO-WAY EULERIAN THIN FILM/DISCRETE PHASE APPROACH PART II: DROPLET BEHAVIOUR IN THE CHAMBER

Andrew Nicoli
Andrew.Nicoli1@nottingham.ac.uk
G2TRC, The University of Nottingham, UK

Kathy Johnson
Kathy.Johnson@nottingham.ac.uk
G2TRC, The University of Nottingham, UK

Richard Jefferson-Loveday
Richard.Jefferson-Loveday@nottingham.ac.uk
G2TRC, The University of Nottingham, UK

ABSTRACT

Within aeroengines, bearing chambers exhibit a highly complex two-phase environment as a result of the complex air/oil interactions. The desire to operate at both higher temperatures and shaft speeds requires sufficient understanding of these systems for design optimisation. Typically, bearings are used to support the radial and axial loads transmitted by the shafts and require oil for lubrication and cooling. These bearings are housed in bearing chambers that are sealed using airblown seals. Efficient scavenging systems ensure that the oil is collected and returned to tank avoiding any unnecessary working of the oil.

Previous work at the Gas Turbine and Transmissions Research Centre (G2TRC) has highlighted the need for an adequate computational model which can appropriately model the oil shedding behaviour from such bearings. Oil can breakup forming droplets and ligaments, subsequently forming thin and thick films driven by both gravity and shear.

The objective of this paper is to explore the modelling capability of fully two-way coupled Eulerian thin film/discrete phase models (ETFM-DPM) applied to our simplified bearing chamber configuration. The models are created using OpenFOAM and two-way coupling is employed, enabling Lagrangian droplets to either impinge on the film surface or be removed through effects such as, film stripping, splashing or edge separation. This paper focuses on the droplets, presenting statistics relating to size, velocity, impingement and residence time and provides insight into solution sensitivity to operational parameters including shaft speed and oil flow rate. This extends upon our previously published work and improves bearing chamber modelling capability.

NOMENCLATURE

Symbol	Description
c_l	Droplet Diameter Coefficient
$\dot{m}$	Mass flow rate, kg/s
k	Distribution Constant
B0, *B1*	Kelvin-Helmholtz Length and Time Coefficients
C0, *C1*	Rayleigh Taylor Length and Time Coefficients
P	Pressure, bar
T	Temperature, K
We	Weber Number
α	Sheltering Parameter
β	Scaling Factor
θ	Diameter, m
μ	Kinematic viscosity, kg/(m.s)
ρ	Density, kg/m^3
σ	Surface tension, N/m
Ω	Rotational speed, rpm
φ	Location Parameter

Acronyms & Subscripts

ETFM	Eulerian Thin Film Model
DPM	Discrete Phase Model
VOF	Volume of Fluid
SST	Shear Stress Transport
sh	Shaft
oc	Outer Chamber

1. INTRODUCTION

Within aeroengines, bearing chambers exhibit a highly complex two-phase environment as a result of the detailed airflow-oil interaction. The demand to operate at both higher temperatures and shaft speeds requires sufficient understanding of these systems for design optimisation.

In general, the flow physics of a bearing chamber can be classified into two separate but interacting regions. Firstly, the shear and gravitational forces drive a segregated flow regime, consisting of laminar wavy oil films ranging from thin to thick. Secondly, the turbulent gas flow transports a dispersed flow region, formed of oil droplets varying in diameter. The segregated flow regime is dependent on not only the amount of oil present but also a balance between the gravitational, viscous and interfacial shear stresses. At lower rotational shaft speeds, the gravitational force dominates over the shear force and a pool regime is observed; oil accumulates toward the bottom of the chamber leading to areas of dry-out on the top walls. As the shaft speed increases, the interfacial shear stress eventually overcomes the gravitational forces and a smooth flow regime is found; the oil begins to rotate in the same angular direction as the shaft and a thinner film is

observed. When transitioning between these two states, i.e. the gravity component and shear effect are equal, a shock regime is observed.

Around the cavity annulus, the local film thickness will influence the amount of heat transfer through the chamber housing. The distribution of film thickness is determined predominantly by the impinging droplets but is also a function of the angular coordinate. The mass and momentum imparted on the film by the droplets is ultimately determined by the initial conditions, namely: the shaft rotational speed, the sealing air flow and the volume flow rate of oil. Therefore, when modelling these systems, it is essential to have accurate data surrounding the droplet initial conditions or an understanding of solution sensitivity to the main parameters.

Glahn et al. [1] were the first to present experimental data measuring droplet diameters and velocities shed from a roller bearing, up to shaft speeds of 16,000 rpm. However, to date, very little additional experimental information quantifying the droplets shed into the bearing chamber is available. As such, it becomes difficult to assess correlations between key parameters, such as droplet size distributions or the impact of shaft speeds and volume flow rate on droplet diameters.

1.1. Bearing Chamber Investigations

Due to the highly complex three-dimensional flow physics observed within bearing chambers, computationally, several different coupled approaches have been developed to model the flow phenomena under investigation. It is important to understand how these approaches can be applied to a bearing chamber and their limitations, as such the following provides a brief summary of the methods for oil droplet modelling and coupled approaches. Part I of our current investigation, [2], explores the methods associated with modelling segregated flow regimes.

Experimental investigations of droplet generation from aeroengine bearings [3–5] has provided a key insight into how, depending on the shaft rotational speed, oil is shed not only as droplet and ligaments into the bearing chamber, but also as sheet formation. Normally for segregated flow regimes, the Volume of Fluid (VOF) approach is well suited, however a major limitation is faced for flow regimes of a mixed nature, i.e. those that include a dispersed phase. Within bearing chamber applications, typically, the droplet diameters observed experimentally are significantly smaller than the standard cell resolutions resolved by a VOF approach. Instead, a discrete phase model (DPM) can be used to more efficiently capture this dispersed flow phase within a Lagrangian reference frame. Adeniyi [6] developed a one-way DPM-VOF approach, including secondary droplet interactions such as splashing. The one-way coupling limited the models capability and was unable to reproduce droplets generated by the separation of the film. Pringuey [7] investigated a two-way VOF-DPM model, within OpenFOAM, to achieve a more efficient atomisation process within aeroengine combustion chambers. More recently, Dick et al. [8] presented a VOF-DPM approach demonstrating a full two-way coupling with an application to a simplified bearing chamber geometry. Dick et al. report good agreement in oil flow patterns but recommend further validation due to limited experimental data.

One of the areas yet to be fully explored is the ETFM-DPM coupling for bearing chamber applications. Previous in-house thin film models developed by Farrall et al. [9] and Wang et al. [10] incorporated droplet impingement models to account for effects such as splashing and absorption. These early models were only able to reproduce smooth flow solutions with numerical difficulties preventing an obtainable solution for shock and pool scenarios. In the Wang thin film formulation, within the energy and momentum equations, the advective terms are simplified and thought to cause these numerical instabilities for shock or pool solutions, in which inertia plays a significant part [11]. Furthermore, in the work of Wang et al. [10], a full two-way coupling between the gas-phase and oil film is not presented; instead, a prior simulation was used to inform the core air flow quantities between the shaft and chamber. As a result, it was found that the shear stresses provided from the air only simulation were not that same as the air shear stresses on the thin film, due to ignoring the oil film interaction. Farrall et al. [12] conducted a DPM study into the effect of droplets on their initial injection conditions for a simplified 2D bearing chamber. Farrall et al. report on the sensitivity of mean droplet diameters on the deposition characteristics, stating that as the mean droplet diameter reduces less splashing is observed.

Chen et al. [13] and the subsequent investigations by Sun et al. [14] also investigated the droplet interactions within an aeroengine bearing chamber environment, within ANSYS CFX. Using a droplet deformation model, the authors investigate the impingement and splash characteristics of particles at different rotational shaft speeds. The deformation of a droplet resulted in a more strongly curved trajectory and a reduced droplet velocity due to the higher drag force experienced. In addition, deformed droplets were more likely to splash. Comparison of results showed that the computational particle trajectories were able to reproduce the experimental trajectories of Sun et al. over a range of operating parameters.

Jingyu et al. [15] successfully demonstrated a fully coupled two-way ETFM-DPM model available within STAR-CD, which, included effects for both a film stripping and an edge separation criteria. Comparison was made to the available bearing chamber investigations of Gorse et al. [16], over realistic engine operating conditions ranging from 4,000 rpm to 16,000 rpm. However, for the computational simulations, the oil film is initialised using a simplified DPM injection around the periphery of the rotating shaft. Whereby droplets are presumed to have an initial velocity equivalent to half of the shaft speed, from which a Rosin-Rammler distribution is also derived. Additionally, Jingyu et al. [17] extended upon this original study and performed simulations using the ETFM-DPM approach for a representative aeroengine bearing chamber, comparing results against in-house experimental data. Here, across all of the rotational shaft speeds and oil flow rates, the computational results were able to accurately predict the film thicknesses, with percentage errors no greater than 10%.

Part I of our current investigation, [2], presents for the first time a fully coupled two-way, transient, ETFM-DPM bearing chamber simulation into the droplet generation process; including accountability for film effects such as both a stripping and an edge separation criteria. The in house OpenFOAM solver, *sprayParcelFilmFoam* [18], was first validated against experimental data for a liquid jet in a high velocity cross flow with excellent agreement for both film thicknesses and particle characteristics. In Part I of this work, a quantitative and qualitative analysis of the film was presented, demonstrating good agreement compared to the experimental data of Hee et al. [4] for shaft speeds up to 12,000 rpm.

The objective of this paper is to, therefore, explore the modelling capability of a fully coupled two-way ETFM-DPM bearing chamber simulation within OpenFOAM and investigate the detailed flow physics. To date, for bearing chamber applications, there are limited experimental studies focused surrounding the rotational shaft speed and the air flow influence on the oil film. However, minimal work has been carried out in order to quantify the droplets and their characteristics that are shed from the bearing into the bearing chamber. A two-way coupling is employed, enabling Lagrangian droplets to either impinge on the film surface or be removed through effects such as, film stripping, splashing or edge separation. This paper will focus on providing accurate droplet statistics and provide knowledge of the solution sensitivity to important parameters. This work will form Part II of our current bearing chamber investigations, expanding upon the previous bearing chamber modelling

capability developed by Nicoli et al. [18] within OpenFOAM, using the existing methodology presented within Part I of our work [2].

2. BEARING SHEDDING RIG

For the purpose of this study, the computational investigation focuses on the aeroengine representative ball bearing presented by both Santhosh et al. [3] and Hee et al. [4], and more specifically, modelling of the front bearing chamber. Figure 1 presents a diagram of the experimental test rig. Part I, [2], summarises the bearing shedding rig and the operating space explored experimentally, including the computational measurement locations referred to as P2 and P4.

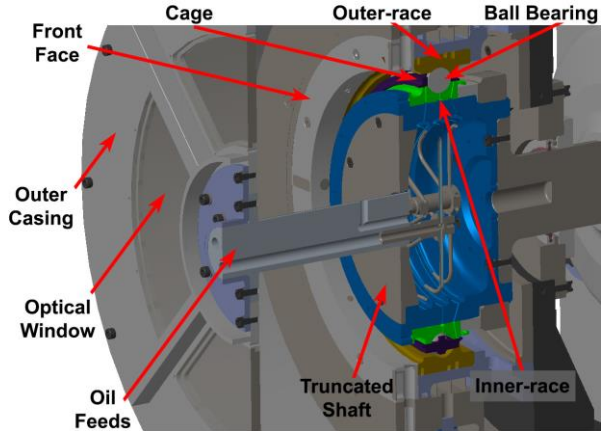

FIGURE 1: SCHEMATIC OF BEARING OIL SHEDDING RIG [4]

The computational grid considered is a hex-dominant mesh created using a cut-cell approach within ANSYS Mesher. A cross-section of the mesh is shown in Figure 2, in total the mesh consists of 35 million cells, with a core cell sizing of 1mm. To ensure sufficient resolution of the oil film, the boundary layer was sufficiently refined over the static outer casing walls where the film develops. Due to its highly complicated nature, the test bearing itself if not modelled, as such the computational domain starts immediately after the ball bearing at the cage. A detailed mesh dependency study is performed in Part I [2].

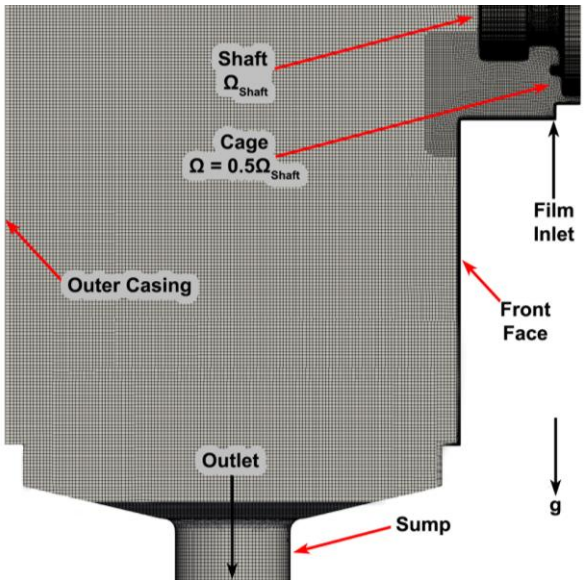

FIGURE 2: CROSS SECTION OF HEX-DOMINANT MESH

Figure 3 shows a cross-section of the ball bearing, highlighting the mechanism for oil film formation on the static outer casing wall. A numerical investigation into the oil inlet boundary condition was performed in Part I of our work [2]. Based on the computational investigation, a representative film inlet boundary condition is implemented. Firstly, it is assumed that all of the oil shed from the cage-edge impinges on the thin film. Subsequently, the film inlet boundary then starts beyond the sharp corner of the outer race, as shown in Figure 3. Therefore, all of the oil entering into the front chamber is introduced as an oil film at this inlet location. The experimental measurements of Hee et al. [4] are used to inform the oil inlet conditions and for closure, a rotational velocity is applied based on the VOF ball bearing investigation of Adeniyi et al. [19].

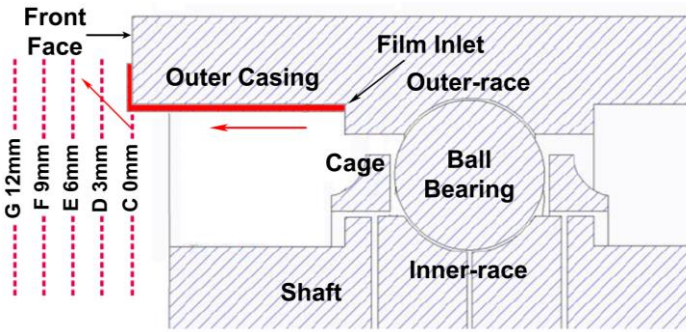

FIGURE 3: CROSS SECTION OF FILM INLET AND AXIAL MEASUREMENT PLANES, MODIFIED FROM [4]

Computationally, all of the oil tracked within the DPM approach is produced as a result of the complex interaction of the air and oil film, this is achieved using a two-way ETFM-DPM coupling. As oil is supplied into the domain via the ETFM inlet, a thin film forms on the surface of the outer casing. Immediately, droplets can be stripped from the surface of the film due to the high shearing gas forces developed from the rotational speed of both the shaft and bearing cage. Once the film reaches the edge of the outer casing and the front face, the momentum of the oil causes it to separate as droplets, whilst a proportion of the film remains attached, flowing down the front face. These droplets travel through the bearing chamber and subsequently impinge on the outer casing walls, forming a thin film, whereby splashing may occur. As these droplets move through the air, the droplet acceleration and slip velocities may result in secondary breakup forming smaller child droplets. As such, the focus of this investigation is to report on the droplet statistics, recorded at measurement planes every 3mm away from the outer casing edge, up to a distance of 12mm. This includes important parameters relating to size, velocity, impingement and residence time, whilst also providing insight into solution sensitivity to operational parameters such as shaft speed and oil flow rate. Overall, the results from this investigation will assist future computational bearing chamber studies and help to provide more realistic oil inlet boundary conditions for the dispersed phase.

2.1. Boundary Conditions

Table 1 summarizes the boundary conditions applied computationally, which are derived from the experimental operating parameters employed by Hee et al. [4]. A full review of the computational boundary conditions are presented in Part I, [2].

TABLE 1: COMPUTATIONAL OPERATING CONDITIONS AND MATERIAL PROPERTIES

Shaft rotational speeds	Ω	5,000 7,000 12,000	rpm
Air temperature	T_a	333.15	K
Oil inlet temperature	T_o	333.15	K
Oil inlet mass flow rates	$\dot{m}_o$	5.2 7.3	l/min
Chamber absolute pressure	P	1.01	bar
Material Properties			
Air density	ρ_a	1.059	kg/m^3
Air viscosity	μ_a	2.008×10^{-5}	kg/(m.s)
Oil density	ρ_o	890.8	kg/m^3
Oil viscosity	μ_o	0.00681	kg/(m.s)
Oil-air surface tension	σ	0.0302	N/m

2.2. Numerical Settings

For the combination of different shaft speeds and flow rates under investigation, each simulation is initialised from the previously validated computational data published in Part I of our work [2]. For this latter work, the same parameter space is investigated, however the focus is aimed on providing an informative analysis of both the thin film formation and its underlying mechanisms. A qualitative examination of the thin film showed that, for all cases investigated, a smooth shear dominated flow regime was observed up to an axial distance of 10mm away from the outer casing front-edge, much like the experimental results reported by Hee et al. [4]. However, moving further towards the film edge and within the P4 counter-current region, a gravity dominated flow regime was observed, leading to a flow reversal and oil being pulled back downward, which mildly persists even up to a shaft speed of 12,000 rpm. Due to the lack of available experimental measurements to compare beyond Plane B, at the 10mm axial location, the results of Nicoli et al. [2] suggested that the presence of both a truncated shaft and the absence of a sealing air flow rate were the underlying determining factors. Unlike a typical high pressure bearing chamber, where the shaft would run throughout, it is suspected that the use of a truncated shaft leads to a reduced shearing velocity toward the front of the chamber and hence an overall reduced shearing force. In addition, experimental studies by Gorse et al. [20] have highlighted the importance of a sealing air flow on the final single phase flow structure; whereby the vortical structure transitions between a rotational speed driven mode (RSDM) to a sealing air driven mode (SADM) upon reaching the critical sealing air flow rate. A quantitative analysis of the thin film was performed, comparing mean film thickness measurements with the experimental data of Hee et al. [4]. Average film thickness measurements were recorded at Planes A and B away front the front-edge showing good results with the experimental data. A trend of decreasing film thickness with an increase in shaft rotational speed was observed; however, with each increase in shaft speed, there was a diminishing return in the reduction of film thickness. Eventually the film thickness becomes independent of the shaft speed, suggesting that for this flow regime observed, there is a minimum average film thickness of 0.4mm. Following the trends noted by Hee et al., extrapolation of the experimental measurement points to 12,000 rpm showed excellent agreement with the computational data across all cases. The work of Nicoli et al. [2] has demonstrated the capability to accurately model the thin film development on the static outer casing walls, such that now, focus can be applied into investigating the droplets that are shed into the bearing chamber; identifying their initial conditions and relevant characteristics.

Within Part I of our investigation, [2], the newly developed in-house OpenFOAM solver *sprayParcelFilmFoam* [18] is used. *sprayParcelFilmFoam* is a transient, fully coupled two-way ETFM-DPM solver with models for both primary atomization and secondary breakup of the particulate cloud. In addition, it includes two-sub models which have been developed and validated for both a film stripping and an edge separation criteria. *sprayParcelFilmFoam* was developed for bearing chamber applications, with an initial validation case study focused on modelling of oil jet-breakup and the subsequent film formation, demonstrating significant improvement over the previous state-of-the-art modelling capabilities [18].

To ensure solution stability, the PIMPLE algorithm is used for the pressure-velocity coupling loop. Convergence of the pressure, velocity and turbulent quantities are assessed using a residual convergence criteria of 1×10^{-6} for the maximum average. Aside from measuring global quantities such as the shaft torque coefficient, convergence is primarily monitored through the DPM oil residence volume. A steady-state solution was assumed once the oil residence volume fluctuated periodically around a fixed average value. In general, a non-time dependent solution was reached beyond a flow time of 1.0s, and a further 1.5s of simulation time was used to temporally average the data; corresponding to 5 full film cycles from inlet to edge. For all pressure, momentum, turbulence and surface film terms, a second order upwind-biased discretization scheme was chosen.

The SST k-ω turbulence model was chosen for all simulations due to its robust formulation and previously demonstrated capability [2], following the work of both Bristot et al. [21] and Singh et al. [22].

2.3. Oil Droplet Modelling

In order to quantify the oil droplets shed into the bearing chamber, it is first important to identify the relevant settings and sub-models that govern the droplet motion. A more detailed analysis, with model equations, can be found in the work of Nicoli et al. [18]. Oil droplets are tracked using a Lagrangian particle tracking approach and in order to account for the particle interactions with the gas-phase, a two-way particle coupling is enabled. Due to the high shearing gas forces, to account for variations in the droplet shape, a dynamic drag model [23] is used instead of the default spherical drag model. An initially spherical droplet moving through a gas phase may become significantly distorted if the gas Weber number is sufficiently large. To account for this droplet distortion, the dynamic drag model linearly varies the drag force from a sphere to a disc based on the particle spherical deviation, which is calculated from the oscillation equations present in the secondary breakup models. The use of a dynamic drag model will also help to better account for the drag on ligaments shed from the front-face edge into the bearing chamber. Whilst these ligaments are not strictly discs, this approach is a necessary approximate to account for their complex and non-spherical shape, as observed experimentally [4].

Secondary Breakup: High shearing gas forces can lead to Kelvin-Helmholtz (KH) and Raleigh-Taylor instabilities forming on the droplet surface. Droplet slip velocities result in KH instabilities, which lead to small child droplets being continuously sheared off the parent droplet. The droplet acceleration results in RT instabilities and given sufficient time these act to completely shatter the droplet. As a result the KHRT model captures a range breakup regimes from low Weber number vibrational breakup up to high Weber number, catastrophic breakup. For the scope of this work, the KHRT breakup model with default model constants is chosen. These consist of a KH length and time coefficient of $B0 = 0.61$ and $B1 = 1.73$ respectively; as well as a RT length and time coefficient of $C0 = 0.5$ and $C1 = 1$.

Particle Turbulent Dispersion: The default method for calculating particle trajectories uses the mean velocity. This ultimately ignores the effect of turbulence on the particle motion and can have a significant impact on the particle path and hence the development of the film. Here, a stochastic discrete random walk approach is used, such that, a Gaussian random number distribution is used to perturb the particle velocity in a random direction.

Splashing: Depending on the droplet Weber number, a parcel may adhere to the film surface or splashing may occur. The Bai splashing model [24] with default coefficients are used, which determines the surface film parcel interaction for both wet and dry surfaces, here partial effects are not included. Both wet and dry surface roughness coefficients need to be supplied, for which the recommended values present by Bai et al. are A_{Dry} = 2630 and A_{Wet} =1320 respectively. Subsequently these surface roughness coefficients are used to determine the critical splashing Weber number for either a wet or dry surface. To resolve the magnitude and direction of splashed droplets, the skin friction coefficient, C_f, also needs to be provided, here a default value of 0.6 is chosen.

Shear Stripping: For a thin film, there is a minimum film thickness and a critical shearing rate beyond which the conditions for shear stripping are satisfied, resulting in the ejection of droplets. A shear stripping criteria is included based on the work of Mayer [25]. The relative velocity between the gas flow and the oil film causes a shearing force at the liquid-gas interface, leading to waves developing on the surface of the film. These waves grow, due to the Kelvin-Helmholtz instability, and form cylinders as the waves roll up. These cylinders are subsequently ejected into the gas phase undergoing further breakup due to Rayleigh-Taylor instabilities resulting in the formation of spherical droplets. As waves form on the fluid surface, the film viscous forces damp them. Mayer determines that by balancing the wave growth with the damping forces, a wave frequency is characterised. For wave growth and eventual break off, this frequency must be greater than zero, resulting in a minimum wavelength for growing waves. As such a sheltering parameter, α, needs to be supplied which defines the proportion of the wave crest exposed to the shearing airflow, here a default value of 0.3 is used. To determine the stripped droplet diameter, a droplet diameter coefficient, C_l, is defined which takes a default value of 3.78. Stripped droplets injected into the gas-phase have an initial velocity and trajectory equivalent to that of the film prior to stripping.

Edge Separation: Over a sharp edge, a proportion of the liquid may either separate from the surface or it may turn the corner and remain attached. The edge separation model of Friedrich et al. [26] is employed, giving a separation criteria based on both a critical wall angle and a critical force ratio. A non-dimensionalised force ratio is derived from a force balance between surface tension, momentum and the acting body forces. For a 90° edge, such as within the bearing chamber, the force ratio is directly proportional to the film Weber number:

$$Force\ Ratio = \frac{We_f}{2} \quad (1)$$

Above a critical force ratio of one, a derived percentage of mass is separated from the film, whilst the rest remains attached. Overall, the mass separated from this film is injected back into the Lagrangian frame of reference as droplets, which by Friedrich's separation model are assumed to have a diameter equal to the separated proportion of the film thickness at the edge. Separated droplets injected into the gas-phase have an initial velocity equivalent to that of the film prior to separation.

3. RESULTS

3.1. Oil Residence Mass

Upon reaching a steady state of the particulate cloud, DPM particle properties were temporally averaged. Table 2 summarises the average particle cloud properties for each rotational shaft speed at a flow rate of 7.3 l/min, distinguishing between both stripped and edge separated particles. For reference, the results at a shaft speed of 7,000 rpm and an oil flow rate of 5.2 l/min are also included. At 5,000 rpm the average total cloud mass, i.e. the sum of both stripped and edge separated particles, is 21.2g, this increases to 27.0g at 7,000 rpm but reduces significantly at 12,000 rpm to just 13.8g. Furthermore Table 3 shows the mass flow rate of oil that is separated as droplets at the front-face edge, compared to the amount of oil supplied into the domain at the film inlet boundary condition. This is then presented as percentage, to therefore demonstrate the proportion of oil that is separated at the edge as droplets. As such, the remainder of oil is either stripped as droplets upstream of the front-face edge or remains attached to the surface and flows down the front-plate.

TABLE 2: AVERAGE CLOUD PROPERTIES AT EACH SPEED

	Film Stripped Droplets			
Shaft Speed (rpm)	**Avg. No. Particles**	**d_{10} (µm)**	**d_{32} (µm)**	**Cloud Mass (kg)**
5,000	42,100	52.6	53.0	2.89×10^{-6}
7,000	2,082,500	58.8	65.9	2.12×10^{-4}
12,000	2,916,200	53.4	56.8	2.12×10^{-4}
7,000 (5 l/min)	496,100	59.8	60.9	1.02×10^{-4}

	Edge Separated Droplets			
Shaft Speed (rpm)	**Avg. No. Particles**	**d_{10} (µm)**	**d_{32} (µm)**	**Cloud Mass (kg)**
5,000	579,200	630	944	21.2×10^{-3}
7,000	292,400	830	1,228	26.8×10^{-3}
12,000	115,100	780	1,049	13.6×10^{-3}
7,000 (5 l/min)	330,348	830	1,179	19.4×10^{-3}

TABLE 3: PROPORTION OF SEPARATED MASS AT EACH SPEED

Shaft Speed (rpm)	**$\dot{m}_{Supplied}$ (kg/s)**	**$\dot{m}_{Separated}$ (kg/s)**	**Percentage (%)**
5,000	0.0965	0.0498	51.6
7,000	0.0965	0.0849	88.0
12,000	0.0965	0.0876	90.8
7,000 (5 l/min)	0.0683	0.0610	89.3

From Table 3, with an increase in shaft speed from 5,000 rpm to 7,000 rpm, the amount of mass separated at the edge subsequently increases from 51.6% to 88.0%. This results in a greater particulate cloud mass at 7,000 rpm, as evident from Table 2. At 5,000 rpm, there are on average a greater number of edge separate particles within the dispersed phase when compared to 7,000 rpm, however this can be accounted for, since these particles are travelling relatively slower due to the reduced gas velocity and therefore have an increased residence time. With an increase in shaft speed to 7,000 rpm, the momentum of the film at the front-face edge increases, hence the amount of edge separation also increases, resulting in a greater proportion of the film height being separated over the edge. An increase in particle diameter can also be associated with the undulation effect observed within the P4 film region, which goes through a maximum at 7,000 rpm, as the flow transitions through the shock regime. Therefore, an overall increase in droplet diameter is observed, evident from the shift in average diameter from 630µm to 830µm. Whilst there are fewer edge separated droplets at 7,000 rpm, this greater droplet diameter, results in an increased cloud mass. Interestingly, a further increase to 12,000 rpm sees a decrease in

particulate mass, Table 2. Here, the increase in shaft speed from 7,000 rpm results in a reduced undulation effect as the film tends to a more uniform smooth shear dominated flow regime, as a result of the higher gas velocity. Whilst a similar proportion of mass is separated at the edge, as apparent from Table 3, these particles are travelling relatively faster and therefore have a shorter residence time, hence, the reduced number of particles produces a smaller cloud mass.

As the shaft speed increases, the amount of film shear stripping that takes place also increases. At a shaft speed of 5,000 rpm, only a very minimal amount of stripping is observed, which is almost negligible in proportion to the total cloud mass. However, even at 7,000 and 12,000 rpm the ratio of mass stripped from the film versus that separated at the edge is still very small, accounting for only 0.8% and 1.5% of the total mass respectively. Whilst there are over an order of magnitude more stripped particles than edge separated particles, at both 7,000 and 12,000 rpm, their average diameter is considerably smaller and therefore only represent a smaller fraction of mass.

Within Table 2 , comparing the two oil flow rates at 7,000 rpm the most noticeable difference occurs within the number of stripped particles present. At 7,000 rpm, stripping predominately occurs within the P4 counter-current region, as a result of the undulation effect, whereas as 12,000 rpm stripping takes place more uniformly around the annulus. Therefore, the reduced number of stripped particles at 5.2 l/min suggests that the undulation effects are not as strong. Table 3 demonstrates that similar amounts of edge separation occurs at both oil flow rates, however, at the flow rate of 5.2 l/min a smaller average diameter is found, which in combination with the reduced undulation effect, overall, results in a reduced cloud mass.

3.2. Oil Distribution

Figure 4 shows a sample of the instantaneous particle trajectories coloured by their particle diameter at a shaft speed of 7000 rpm and a flow rate of 7.3 l/min. The snapshot is taken after one complete film cycle to best visualise the particle trajectories. As time progresses, particles from the top of the chamber fill the rest of the domain.

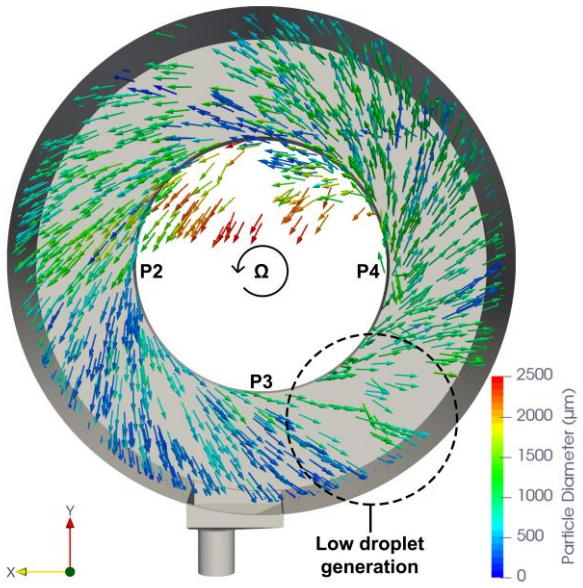

FIGURE 4: INSTANTANEOUS PARTICLE TRAJECTORIES WITHIN THE MAIN CHAMBER COLOURED BY DIAMETER FOR 7000 RPM 7.3 L/MIN

Moving around the chamber annulus, it is immediately clear that the droplet diameter distribution changes significantly as a function of the angular coordinate. To understand the effects more clearly, it is important to analyse the underlying flow physics within each 90° quadrant, therefore we start from the P2 region and move anticlockwise with the direction of shaft rotation. Additionally, Figure 5 shows the mean film Weber number as a function of the angular coordinate for the three shaft speeds investigated at 7.3 l/min. The results within Figure 5 are presented at the front-face edge, Plane A in Figure 3, i.e. the location at which the film separates into the main chamber. The film Weber number is directly proportional to the critical force ratio required for edge separation, whereby separation begins above film Weber number of 2. Due to the highly transient nature of the film, the maximum and minimum Weber numbers are also presented, at 7,000 rpm, to demonstrate the possible range in edge separation. For the P2 sector within Figure 5, a local maximum in film Weber number is observed, as we increase the shaft speed from 5,000 rpm to 12,000 rpm, this maximum shifts further around the annulus from 70° to 130°. Here, the film velocity travels in the direction of gravity and subsequently gains sufficient momentum for it to fully separate over the edge into the bearing chamber, as observed from the instantaneous film thickness measurements on the front-face wall presented in Part I, [2]. With respect to the rest of the oil film around the chamber annulus, the higher film velocity produces a relatively thinner film. At the point of edge separation, based on the formulation of the Friedrich's separation model, these edge separated droplets are given a diameter equivalent to the film thickness removed from the surface. From Figure 4, droplets are seen to shed from the edge with an average particle diameter close to 500μm and a minimum of 200μm.

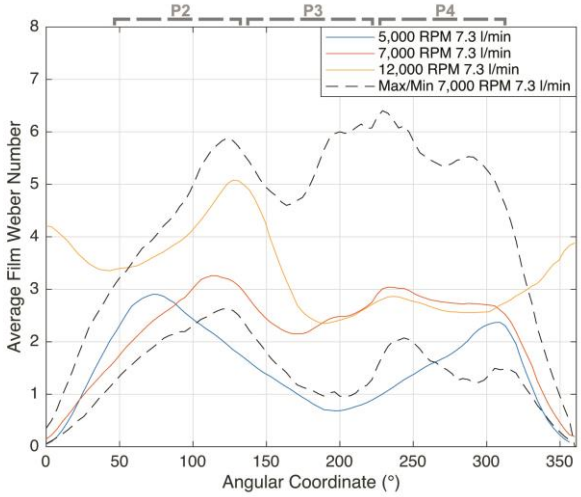

FIGURE 5: MEAN FILM WEBER NUMBER WITH ANGULAR COORDINATE AT THE EDGE (7.3 L/MIN)

Moving from the P2 region towards the bottom of the chamber at 180°, the P3 quadrant a reduction in film Weber number is observed. The film velocity begins to slow leading to a gradual increase in film thickness and hence an increase in particle diameters separated over the edge. However, as the film Weber number reduces, the amount of edge separation also decreases, resulting in a proportion of the film starting to remain attached as it flows over the edge; this happens when the Weber number drops below 2. For all of the shaft speeds investigated this effect becomes the greatest, just after the bottom dead centre location, at around 190°, as evident in Figure 5. The smooth shear dominated flow regime starts to transition into a gravity dominated flow

regime, whereby the film begins to pool at this location. At the 190° location, a large proportion of the mass remains attached as it turns the corner, with only a small amount of droplets being periodically separated, apparent by the lack of particles captured within the instantaneous particle trajectories of Figure 4.

As shown in our previous work [18], moving into the P4, counter-current region, upstream of the edge, at an axial distance of 10mm from the front-face edge, the film travels in the opposing direction of gravity, representative of a smooth shear dominated flow regime; observed experimentally by Hee et al. [4]. However, as we move closer to the edge, the effects of gravity begin to dominate as the fluid slows, changing in direction, as it is pulled back downward; this phenomena mildly persists even up to a shaft speed of 12,000 rpm. The film begins to accelerate downward, intermittently undulating, due to the axial displacement of the incoming upstream fluid. This effect causes a build-up of fluid, increasing the film thickness and as a result relatively larger particles are seen to shed from this rising side of the chamber in Figure 4; resulting in an average particle diameter of approximately 1000μm. At the front-face edge, the undulating effect observed computationally reaches a maximum at a shaft speed of 7,000 rpm [2].

Progressing towards the top of the chamber, the P1 region, the film begins to transition back towards a smooth shear dominated flow regime as the angle with respect to gravity changes. From Figure 5, it is clear that at the two shaft speeds of 5,000 and 7,000 rpm, the mean film Weber number reduces significantly, reaching a minimum at the top dead centre location. As such, the amount of edge separation consequently reduces, becoming zero at the 0° location. Here, at the edge, the film remains attached, flowing radially outward over the front-face surface. The reduced film velocity and further influence of gravity causes the film to quickly build-up at this location. Eventually, as the film accumulates and the relative velocity between the thin film and high shearing air flow increases, such that the critical conditions for shear stripping at this location become satisfied. As a result a small number of large diameter particles are seen to be stripped from this location, with diameters up to a maximum of 2,500μm. Due to the formulation of the stripping criteria, these particles are prescribed an initial velocity and trajectory equivalent to that of film from where they are stripped from, hence have a small velocity component. These larger heavier particles are therefore seen to fall under the effects of gravity, as shown in Figure 4, instead of being transported by the gas flow. An equivalent effect is also observed within the P4 side, whereby a very small number of particles are seen to be moving with a negative tangential velocity with respect to the bulk flow. Similarly, these are particles stripped from the front-face surface due to the accumulation of film as it flows around the edge, although this occurs much less frequently. At the top of the chamber, for a shaft speed of 12,000 rpm this stripping phenomena still occurs, but with a much reduced frequency; since a greater proportion of the fluid is able to separate over the front-face edge. This results from the film being able to reach a more uniform smooth shear dominated flow regime beyond the 270° angular location as previously discussed in Part I [2], which is apparent by the film Weber number profile captured within Figure 5. Similarly, beyond the 0° location, at the two 5,000 rpm and 7,000 rpm shaft speeds, the film Weber number begins to increase again, and edge separation resumes as we move back towards the P2 region.

Within Figure 4, toward the top of the chamber, there are a small fraction of particles with a diameter less than 100μm. These particles differ to the previously mentioned edge separated particles, which have a minimum diameter of 150μm. At the top of the chamber, these particles originate further upstream of the front-face edge, resulting from the shear stripping of the thin film. In fact, at a shaft speed of 7,000 rpm, these particles emerge as a result of the undulation effect observed within the P4 counter-current region. This effect causes a thickening of the film toward the edge and the critical conditions for shear stripping take place. These particles are heavily influenced by the core air flow and by the time they reach the main chamber are seen travelling through the P1 region in Figure 4. At a shaft speed of 7,000 rpm shear stripping of the film is only observed to take place within the P4 region. At the slower shaft speed of 5,000 rpm, virtually no shear stripping takes place, as apparent by the particle cloud statistics reported in Table 2; in part due to the lower shaft speed but more importantly due to the undulation effect approaching a maximum around a shaft speed of 7,000 rpm. As we progress to the higher shaft speed of 12,000 rpm, shear stripping takes place more uniformly around the bearing chamber annulus as the relative velocity between the thin film and gas flow increases. This results in a more uniform dispersion of stripped particles around the annulus within the main chamber compartment.

Since the origin of these stripped is located upstream on the front-face edge, experimentally, it may be possible to introduce a baffle in order to block these stripped particles; providing an opportunity experimentally to distinguish between the edge separated and stripped particles.

3.3. Quantified Particle Trajectories

Figures 6a-c shows a more detailed break-down of the particle trajectories in the tangential/radial plane. The front-face edge, where separation occurs is shown by the inner black circle, whilst the chamber outer casing is depicted by the outer black circle; the space is further subdivided the blue dashed lines for viewing clarification. Figure 6a shows the trajectories for 5,000 rpm and the following images are for 7,000 rpm and 12,000 rpm respectively. For each rotational shaft speed particle trajectories are considered at 4 discrete locations around the annulus to better assess the trajectory dependence on both angular coordinate and particle diameter.

Moving around the chamber annulus, starting at the P2 position for 5,000 rpm, the smaller particles are seen to be deflected more heavily by the gas flow compared with the larger diameter particles. Increasing the shaft speed to 7,000 rpm, the same effect is observed however upon reaching 12,000 rpm little deflection is seen, as particles separate with a very high tangential component. A similar trend is observed at the P3 location, however compared to the smaller particles, the larger diameters have a greater radial component due to film velocity slowing and the effect of gravity beginning to dominate. This again carries forward to the P4 location, whereby within the film, the gravity dominated flow regime occurs. As the film is pulled back downward due to gravity, the film tangential component reduces in relation to the radial component. This is most notable at 7,000 rpm where the undulation effect reaches its maximum and subsequently diminishes with an increase in speed up to 12,000 rpm.

The most notable difference in particle trajectories occurs within the P1 region, and for simplification only the edge separated particles are shown. Therefore, not highlighting the previously discussed stripped particles over the front-face surface, which can range in diameters up to 2,500μm as shown in Figure 4. At the top of the chamber the spread in particle trajectories is the greatest. For the two slower shaft speeds, the larger particles are seen to deflect heavily downwards with a reduced tangential velocity component. This is associated with the film velocity rapidly reducing towards the 0° location on the front-face edge, as discussed in Figure 5. These particles are subsequently carried by the gas flow but are heavily influenced by the effect of gravity, ultimately causing them to arc downwards into the P1 sector. At 12,000 rpm, as a more uniform smooth shear dominated flow regime is achieved, this phenomenon ceases and, in general, around the chamber annulus the particle trajectories are consistent.

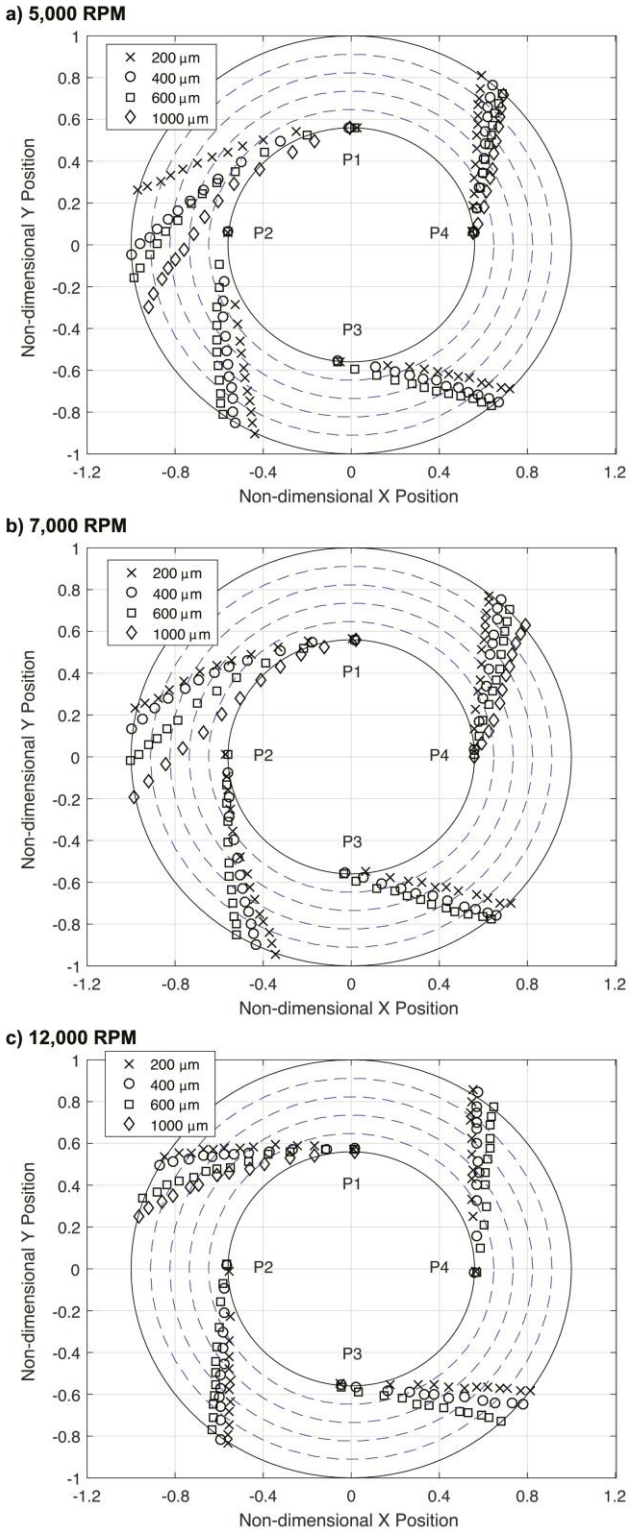

FIGURE 6: EDGE SEPARATED PARTICLE MEAN TANGENTIAL TRAJECTORIES FOR EACH SHAFT SPEED (7.3 L/MIN)

The classification of particles shed from the P1 region has an important impact on interpretations of experimental proceedings. It has been identified that these large diameter particles, either edge separated or stripped, will have trajectories passing through the P2, co-current region. Computationally, this occurs at shafts speeds below 7,000 rpm and therefore falls within the experimental parameter scope. Within the experiment, the high-speed imaging configuration can only consider one quadrant at a time. Therefore, experimentally, when assessing the P2 region it is important to recognise that some of the larger, heavier, particles may originate from the P1 section. This will become critical when trying to assess either particle diameter histograms within a specific quadrant, or when using image processing to determine particle trajectories; since these particles will not be travelling with the bulk of the flow and their subsequent interactions should be carefully considered. Ideally, a two component Phase Doppler Particle Analyser (PDPA) could be used instead to capture the full droplet distribution.

Figure 7 shows the averaged particle trajectories in the radial/axial plane for each shaft speed, at 7.3 l/min, however only the trajectories for the P2 and P4 regions are shown. The P1 and P3 trajectories are not shown for simplification, although both regions have very similar trajectories and lie approximately half-way in between the P2 and P4 paths shown in Figure 7. Across all of the simulations, there was a negligible difference in the radial/axial trajectory as a function of particle diameter. Within the non-dimensionalised radial plane, particles start at the front-face edge and terminate on the main chamber outer wall; and within the non-dimensionalised axial plane, the 0 location corresponds to the front-face edge and extends the whole axial length of the domain.

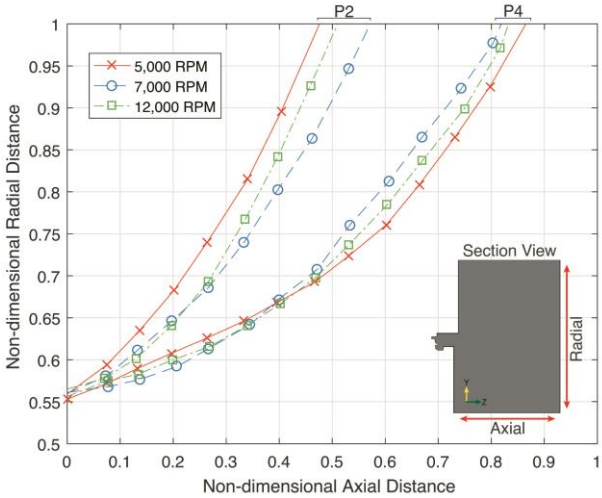

FIGURE 7: RADIAL/AXIAL EDGE SEPARATED PARTICLE TRAJECTORIES BASED ON AVERAGE PARTICLE DIAMETER

Within Figure 7, considering the P2 or P4 particles trajectories independently, for all of the shaft speeds investigated, there is neither a clear increase or decrease in the axial trajectory of particles with the shaft speed. All of the particles around the chamber annulus, impinge directly on the outer cylinder chamber wall, never reaching as far as the front-facing viewport windows, as seen in Figure 1; this is also evident experimentally, due to lack of an oil film on these optical windows [4]. On the outer chamber annulus, the majority of the oil film therefore resides between a non-dimensional axial distance of 0.45 to 0.85. After sufficient time, within the lower half of the chamber, oil fills the space up to the non-dimensional distance of 0.45, due to the attached film flowing over the front-face edge as previously reported computationally [2]. On the outer cylinder wall, as the film begins to accumulate, the shearing air flow and gravity causes it to pool towards the sump, where it is eventually gravity scavenged. However, as the oil film develops on the outer wall, the axial momentum of the impinging film fills the remain gap between the non-dimensional distance of 0.85 and 1. Clearly

outside of this axial extent there exists a dry-out region, namely for the initial 0.45 non-dimensional axial distance within the top half of the outer chamber annulus. In terms of heat transfer, for an aeroengine bearing chamber application, this may present a significant problem leading to extremely hot regions. Subsequently, any small amounts of oil impinging on these regions could rapidly degrade leading to effects such as coking.

3.4. Particle Diameters

The following sections consider a quantitative analysis of the particle statistics into the main chamber. Figure 8 shows the particle diameters resulting from the shear stripping effect which takes place upstream of the expansion edge. Results are shown for a shaft speed of 7,000 rpm at 7.3 l/min, however very similar diameter distributions are observed over all cases in which shear stripping takes place. A bin width of 2µm is chosen and the data is presented as a normalised probability distribution, such that the sum of all the bins is equal to a probability of one. The stripped particles are sampled as they pass through Plane A at 0mm.

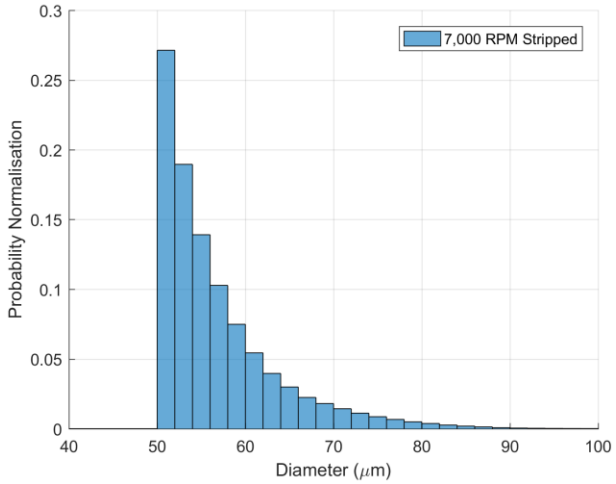

FIGURE 8: NORMALISED STRIPPED PARTICLE DIAMETERS AT 7,000 RPM AND 7.3 L/MIN

The stripped particle diameters follow a log-Rosin-Rammler distribution, otherwise known as a Gumbel distribution which typically favours an extreme value. For a log-Rosin-Rammler distribution, the probability density function usually takes the following formula:

$$F(x;\varphi,\beta,k) = \frac{k}{\beta}e^{-(z+e^{-z})} \quad \textbf{(2)}$$

Where, $z = \frac{x-\mu}{\beta}$, such that φ is the location parameter, β is the scaling factor and k is a constant. For the stripping histogram, shown in Figure 8, these constants are $\varphi = 51$, $\beta = 4$ and $k = 3$, for $x = 0{:}100$. The minimum diameters observed within Figure 8, was 50µm up to a maximum diameter of 90µm, resulting in an average particle diameter of 55µm. However, it should be noted that, for the cases investigated at shaft speeds where sufficient stripping takes place, the smallest diameter actually stripped from the surface of the film was 40µm. These smaller diameters followed the same log-Rosin-Rammler distribution, i.e. extrapolating backwards there were exponentially more particles at 45µm than 50µm and the same again at 40µm.

However, the sheer quantity of particles less than 50µm caused severe numerical difficulties, resulting in an extremely large calculation time per time step, ultimately causing the simulation to stall. At a shaft speed of 7,000 rpm, the average cloud mass represented by the stripped particles accounts for less than 1% of the total cloud mass. Subsequently even though there are significantly more particles less than 50µm, due to the smaller diameter, their mass makes up a small proportion of the total stripped mass and an even smaller percentage of the overall cloud mass. Therefore, in order for simulations to run efficiently, it was discerned that a limit on the minimum stripped particle diameter was required and set to 50µm. In an effort to conserve mass, stripping is still able to take place below this limit, although particles are immediately transferred to the gas phase using an in-built density correlation available within OpenFOAM. As such, the gas phase density is adjusted accordingly, effectively treating these particles as a fine oil mist. However, due to the very small mass associated with these droplets, the overall change in gas density is almost negligible and is immediately dissipated.

Figures 9a-d, show the normalised probability distributions for edge separated particle diameters at each shaft speed and an oil flow rate of 7.3 l/min; for comparison the 7,000 rpm 5.2 l/min case is also included. The particle statistics are recorded at the point of edge separation, i.e. along plane A at 0mm, in order to provide accurate data surrounding the particle initial conditions. For simplification, due to their relatively larger diameters, the previously discussed particles that are stripped from the P1 front-face surface are also included in the following particle diameter histograms. The histograms within Figures 9a-d, have a bin width of 50µm.

At a shaft speed of 5,000 rpm, as in Figure 9a, a similar log-Rosin-Rammler distribution is also observed for the edge separated particles. Much like the stripped particle diameters, the distribution is positively skewed but with less weight towards the extreme value. Following equation 2, this results in the constants $\varphi = 475$, $\beta = 225$ and $k = 45$, for $x = 0{:}2000$. At 5,000 rpm these edge separated particles, have a minimum diameter of 150µm up to a maximum of 1,800µm resulting in an average diameter of 630µm. These particles close to the maximum diameter range are representative of the ligaments observed experimentally [4], which is true for all shaft speeds investigated computationally. Interestingly, across all of the shaft speeds and flow rates investigated the smallest edge separated particles observed are never less than 100µm. This shows that there is a distinct region in which there is no overlap between edge separated and stripped particle diameters. As the rotational shaft speed is increased to 7,000 rpm, Figure 9b, the log-Rosin-Rammler distribution shifts to a positively skewed bimodal distribution, with clear peaks at both 300µm and 900µm. The same is true at the lower oil flow rate of 5.2 l/min, within Figure 9d, although in contrast, the distribution is negatively skewed with distinct peaks at 450µm and 900µm. However, both oil flow rates at the 7,000 rpm share the same average particle diameter of 830µm and with a maximum of 2,500µm. The bimodal distribution can be understood from the film formation prior to separation in Part I, [2]. Within the P2 co-current region, the fully smooth shear dominated flow regime at the front-face edge produces a relatively faster and hence thinner film. This is represented by the diameters shed into the main chamber, forming a peak around a diameter of 300µm. Moving around the annulus to the counter-current, P4, region the undulation effect which reaches a maximum around 7,000 rpm results in a comparatively thicker film. The undulation effect causes significant variance within the particle diameters observed, resulting in a distinct peak at 900µm. Moving to the highest shaft speed, Figure 9c, the bimodal distribution shifts back towards the log-Rosin-Rammler distribution, although this time, slightly skewed to the extreme value, which peaks at a diameter of 600µm. The resultant average particle diameter is 780µm with a maximum diameter 2,150µm. A reasonable fit to the probability

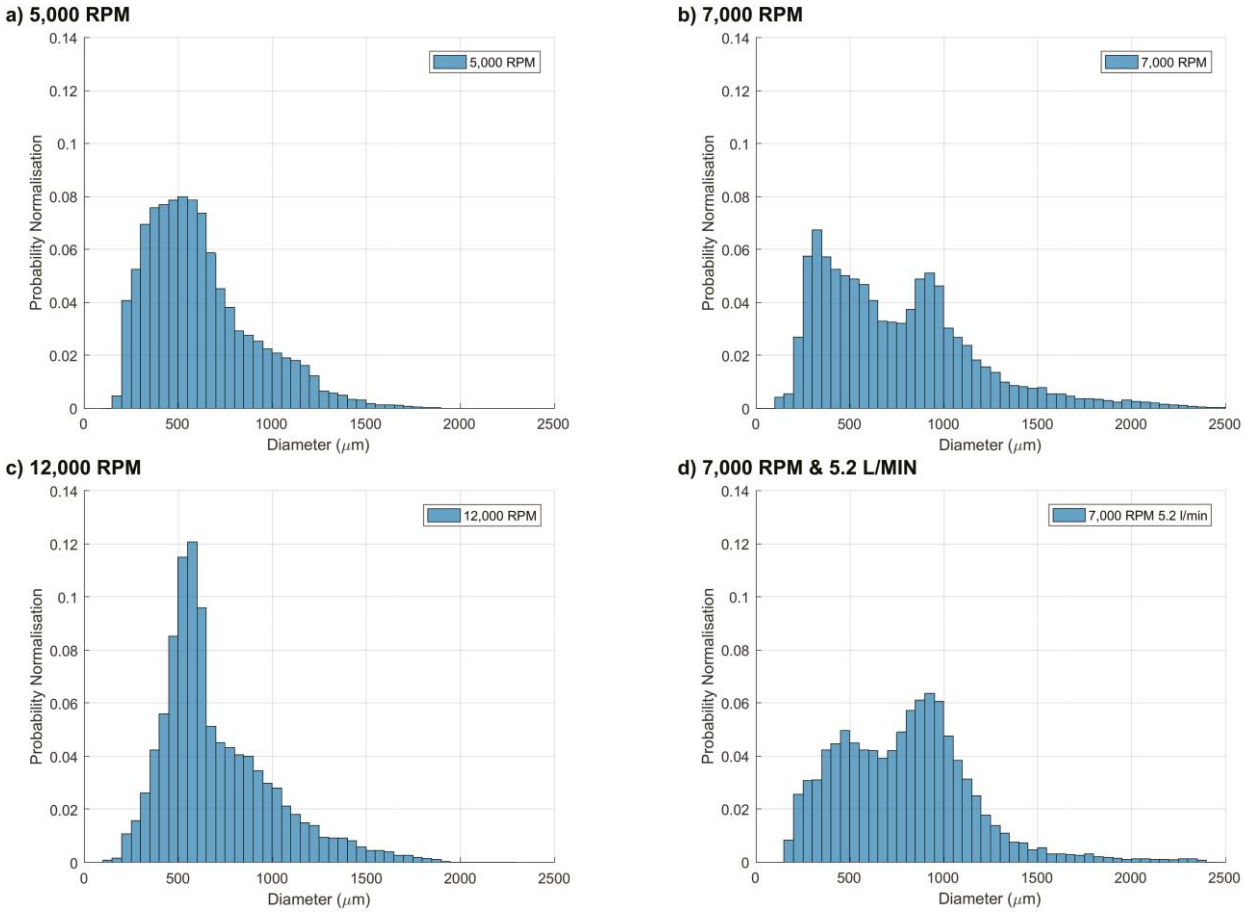

FIGURE 9: NORMALISED EDGE SEPARATED PARTICLE DIAMETERS AT EACH SHAFT SPEED

distribution described in equation 2 can be achieved using the constants $\varphi = 600$, $\beta = 250$ and $k = 45$, for $x = 0{:}2000$.

Interestingly, the only cases to experience any secondary break-up of the particulate cloud were for the two oil flow rates at the shaft speed of 12,000 rpm. Figure 10 shows a comparison of the original particle diameters at the 0mm plane versus the result of secondary breakup within the particulate cloud at plane E, 12mm away from the front-face edge. A similar result is also observed for the second flow rate at 5.2 l/min. Beyond the 12mm plane, the amount of secondary breakup reduces significantly, and little change is seen. From Figure 10, it is clear that only minimal secondary breakup occurs, mainly due to the Kelvin-Helmholtz instabilities formed by the droplet slip velocities. Whereas it appears that there is not sufficient time or acceleration for the Rayleigh-Taylor instabilities to fully develop, which ultimately shatter the droplet into many smaller ones. The main shift in diameters is observed for the largest particles greater than 1250µm and also for particles with the range of 700µm to 900µm; ultimately this results a greater number of particles within the 450µm to 650µm range.

Based on the previous observations presented by Nicoli et al. [2], it is unsurprising that within the main chamber there is minimal particulate breakup. Within the experimental test rig configuration, it is suspected that the presence of a truncated shaft leads to a reduced shearing velocity within the air flow and the lack of a sealing air flow further compounds this issue. As such, the shearing velocity within the main chamber will be reduced in comparison to that of a real aeroengine bearing chamber where significant breakup of the particulate cloud might be expected.

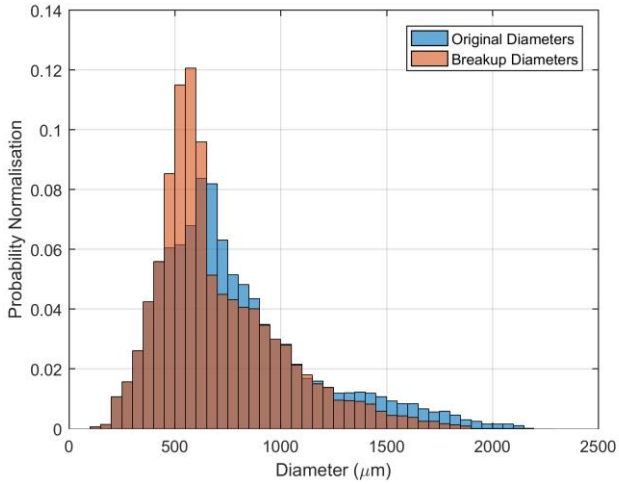

FIGURE 10: COMPARISON OF SECONDARY BREAKUP FOR THE PARTICULATE FLOW AT 12,000 RPM (7.3 L/MIN)

3.5. Particle Velocities

Figures 11a-c show contour maps of edge separated particle diameters against velocity magnitude, for shaft speeds at 5,000 rpm, 7,000 rpm and 12,000 rpm respectively, and an oil flow rate of 7.3 l/min. The contour maps are separated into individual bins, coloured by the normalised probability distribution, such that the total contour area sums to one. Results are recorded at plane E, 12mm from the front-face edge, although similar results are observed for planes closer to the edge.

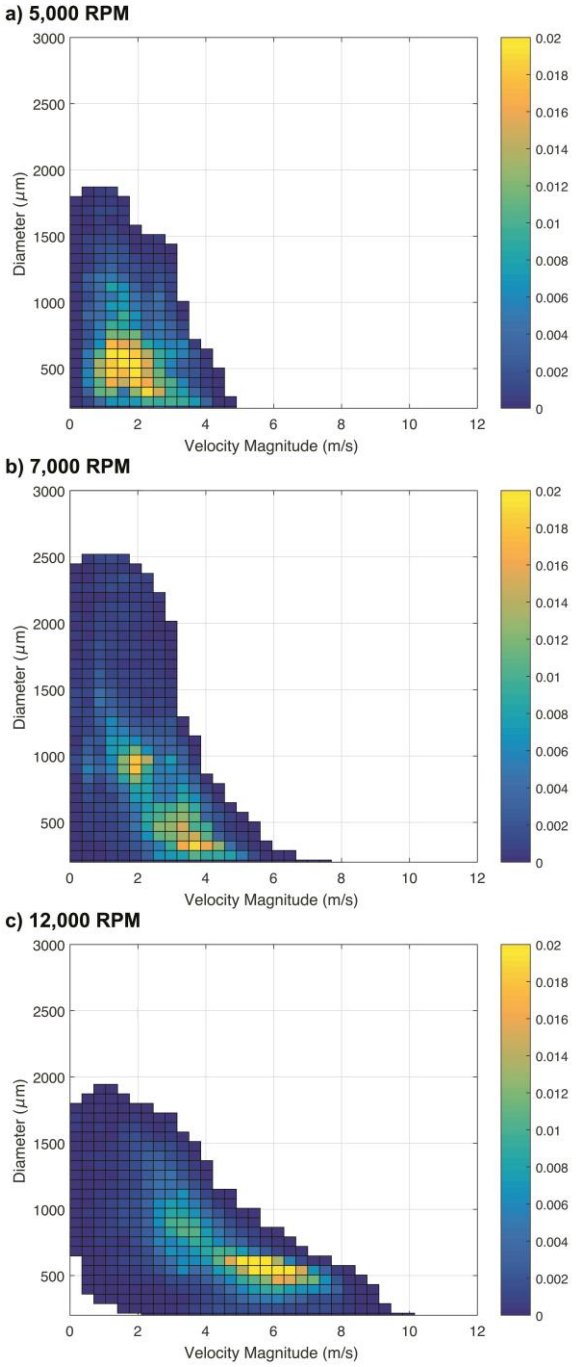

FIGURE 11: CONTOUR MAP OF PARTICLE DIAMETER VERSUS VELOCITY COLOURED BY NORMALISED PROBABILITY

Within Figure 11a, at 5,000 rpm, it is clear that the maximum edge separated diameter peaks at 1,800μm in line with the diameter distribution presented in Figure 9a. It is also clear that, the highest frequency of particles resides within the diameter range between 350μm to 650μm. The bulk of these particles separate with a mean velocity magnitude in the range of 1.0 to 2.5 m/s. At 5,000 rpm, the fastest moving particles observed have a velocity magnitude no greater than 4.5 m/s. Overall, there is a clear correlation between the smaller diameter particles having a greater velocity magnitude compared with the larger diameter particles which move at a relatively slower velocity; this trend applies for all of the shaft speeds investigated.

With an increase in shaft speed to 7,000 rpm, Figure 11b, a notable increase in the maximum particle diameter is seen, as a result of the increasing undulation effect within the P4 region. Two distinct peaks are identifiable within the contour map of Figure 11b, for particle diameters at 900μm and 300μm, characteristic of the bimodal distribution presented in Figure 9b. At these two points, particles reach a velocity magnitude of approximately 2 m/s and 3.5 m/s respectively. The smaller, faster moving particles are representative of the fluid separated within the P2 side, and conversely the larger, slower particles for the counter-current P4 region. Overall, at 7,000 rpm the maximum velocity of the particles is around 7.5 m/s.

At a shaft speed of 12,000 rpm, Figure 11c, the maximum diameter reduces back down to a value of 1950μm, as the undulation effect reduces and secondary break-up begins. An overall increase in particle velocity magnitude is observed, with the highest frequency of particles clustered at a diameter of 500μm and a velocity magnitude of approximately 6 m/s. At 12,000 rpm the maximum recorded velocity magnitude is 10 m/s.

Considering Figures 11a-c, a general trend of increasing average particle velocity with an increase in the rotational shaft speed can be observed. However, it is important to note that this is also a function of the angular location around the chamber, which can heavily influence both the size and velocity of the edge separated particles. This is particularly true of the P4, counter-current region, where a gravity dominated flow regime is observed close to the front-face edge. This is most noticeable around 7,000 rpm, whereby the undulation effect reaches a maximum, subsequently decreasing towards 12,000 rpm.

3.6. Particle Residence Time

Figure 12 shows the average residence time recorded for particles immediately before impingement on the outer chamber wall at shaft speeds: 5,000 rpm, 7,000 rpm and 12,000 rpm and a flow rate of 7.3 l/min. Results are only shown for the flow rate of 7.3 l/min however very similar trends and values are also observed at the lower oil flow rate. Diameters are included for both stripped and edge separated particles.

For all of the shaft speeds investigated, it is immediately clear that with an increase in particle diameter, the final residence time of the particles increases. Furthermore, within this flow regime observed, there are no particles exceeding a residence time of 0.2s, with a minimum residence time of at least 0.05s. At 7,000 rpm and 12,000 rpm, within Figure 12, the residence time for stripped particles less than 100μm are also shown. Interestingly, the stripped particles experience a very similar residence time compared with the small diameter edge separated particles at 150μm. It is suspected that since these stripped particles, which originate within the film upstream of the front-face edge, travel with a faster velocity. This, in combination with being relatively smaller in size, should result in a shorter residence time. However, these particles are influenced more strongly by the gas flow, resulting in longer particle trajectories and hence residence time. From the stripped particle residence time, it is also clear that these particles

are not captured within regions of recirculation, as indicated by the lack of a noticeable increase in residence times. This suggests that there is not a concern for oil degradation due to smaller droplets undergoing significant heating whilst being entrained within the air flow.

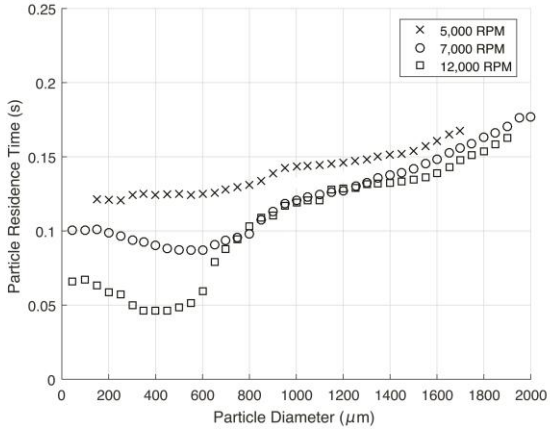

FIGURE 12: AVERAGE PARTICLE RESIDENCE TIME IMMEDIATELY BEFORE IMPINGEMENT ON THE OUTER CASING WALL (7.3 L/MIN)

For the edge separated particles, at the two higher shaft speeds, initially there is a clear decrease in residence time with an increase in particle diameter up to approximately 400μm, especially at 12,000 rpm, although this is not observed for a shaft speed of 5,000 rpm. Beyond this diameter range, over all shaft speeds investigated, the residence time is seen to increase with the particle diameter. For diameters exceeding 700μm, almost identical residence times are observed for the shaft speeds at both 7,000 rpm and 12,000 rpm. When considering diameters below 700μm, as expected, there is a decrease in particle residence time with an increase in shaft speed; however, beyond this diameter range, it is clear that increasing the shaft speed starts to have a less significant impact on the residence time. It is also important to consider the particle residence time as a function of the angular location. As observed in Figure 7, particles shed from the P4, counter-current region, travel a greater axial distance compared with the co-current P2 region. Furthermore, at slower shaft speeds, particle trajectories towards the top of the chamber, experience a greater influence of gravity, resulting in a reduced tangential trajectory as they travel through the P2 region, Figure 6. In Figure 4 it is also witnessed that particles are stripped from the front-face surface within the P1 region, which tend to fall slowly under the influence of gravity. In addition, within Figures 11a-c, the relative increase in particle velocity with shaft speed is small for the larger diameter particles, above 1000μm. As such, when incorporating all of the different flow physics observed around the chamber annulus, the reasons for the increase in particle residence time with diameter start to become apparent, highlighting the vast complexity of the problem.

For future bearing chamber simulations, it would be ideal to provide a DPM inlet boundary condition at the front-face edge, to account for both the edge separated and film stripped particles exiting into the main chamber compartment. This would remove the need for modelling the thin film formation which develops as a result of oil exiting from the ball bearing; hence significantly reducing the computational cost associated with resolving the mesh within this region and the associated two-way ETFM-DPM coupling required, such as either film stripping or edge separation. However, from the DPM analysis presented here, it is clear that the mechanisms for both edge separation and film shear stripping are influenced by many different parameters around the chamber annulus. As such, due to the detailed flow physics observed within the present computational investigation, it may become extremely difficult to successfully represent this type of boundary condition and care should be taken to provide both accurate particle and thin film statistics.

4. CONCLUSIONS

Extending on the current computational study in Part I, [2], the fully coupled two-way ETFM-DPM solver, *sprayParcelFilmFoam*, has been successfully applied to a representative bearing chamber geometry. A detailed analysis of the particles shed into the bearing chamber is carried out, providing insight into new flow physics for aeroengine bearing chamber modelling. Numerical studies are performed for a combination of three different rotational shaft speeds and two oil flow rates.

Accurate particle statistics are provided surrounding the droplet conditions as they are shed into the main chamber compartment and an understanding of solution sensitivity is provided. Qualitatively, the distribution of oil resulting from the mechanisms of edge separation and film shear stripping are presented and analysed, giving insight into the dependence on both shaft speed and angular location around the chamber annulus. It is observed that particles separated within the P2, co-current region, are relatively smaller and faster than the P4, counter-current region, due to the differences in flow regimes observed for the thin film. A smooth shear dominated flow regime is observed at P2, whereas a gravity dominated flow regime is detected at the edge of the P4 region, which mildly persists even up to a shaft speed of 12,000 rpm.

At slower shaft speeds, the effect of a gravity driven flow regime continues towards the top of the chamber at P1. This causes a significant reduction in film velocity and particles are shed with a reduced tangential trajectory. Subsequently, these particles are observed travelling through the P2 region and can therefore have a significant impact on experimental results if not accounted for. At 12,000 rpm, as the gravity driven flow regime diminishes, this effect also reduces. Furthermore, toward the top of the chamber, as fluid remains attached over the front-face edge, it accumulates before being stripped as large diameter particles, up to a maximum of 2,500μm, which consequently fall under the influence of gravity.

A quantitative analysis of particle diameters is presented. A distinct split between edge separated and stripped particles is observed. Stripping only occurs at shaft speeds greater than 7,000 rpm, for which their distribution follows a log-Rosin-Rammler profile, resulting in an average particle diameter of 55μm and a maximum of 90μm. At both 5,000 rpm and 12,000 rpm, a log-Rosin-Rammler distribution is also observed for the edge separated particles. In general, the edge separated particles have a minimum diameter of 100μm, which ranges up to a maximum of 2,500μm. For the oil flow rates at 7,000 rpm, a bimodal diameter distribution is observed, with two distinct peaks around 300μm and 900μm. Analysis of diameter distributions within each quadrant revealed this to be a result of the difference between the P2 and P4 co/counter-current regions; whereby at 7,000 rpm, the undulation effect reaches a maximum. Minimal secondary breakup of the particulate cloud is only experienced at 12,000 rpm, suspected to be as a result of the presence of a truncated shaft and the lack of a sealing air flow throughout the chamber, in comparison to a more representative aeroengine bearing chamber. A general trend of increasing particle velocities with shaft speed is also observed. Particle residence times are seen to increase with particle diameter; however, beyond a diameter of 700μm very similar residence times are observed across all shaft speeds. Overall, it is clear that there are a few different parameters around the chamber annulus that influence the mechanisms for particle formation, including: shaft speed, angular location and the film flow regime.

ACKNOWLEDGEMENTS

This project has received funding from the Clean Sky 2 Joint Undertaking under the European Union's Horizon 2020 research and innovation programme under grant agreement No 724625. The authors are grateful for the technical and financial support provided by Rolls-Royce. In addition, the authors acknowledge the use of the University of Nottingham High Performance Computing Facility as well as access to Athena at HPC Midlands+, which was funded by the EPSRC on grant EP/P020232/1.

REFERENCES

[1] A. Glahn and S. Wittig, "Two-Phase Air/Oil Flow in Aero Engine Bearing Chambers: Characterization of Oil Film Flows," *J. Eng. Gas Turbines Power*, vol. 118, p. 578, 1996.

[2] A. Nicoli, K. Johnson, and R. Jefferson-loveday, "Simulation Of A Simplified Aeroengine Bearing Using A Fully Coupled Two-Way Eulerian Thin Film/Discrete Phase Approach Part I: Film Behaviour Near The Bearing," *J. Eng. Gas Turbines Power*, 2020.

[3] R. Santhosh, J. L. Hee, K. Simmons, G. Johnson, D. Hann, and M. Walsh, "Experimental Investigation of Oil Shedding From an Aero-Engine Ball Bearing at Moderate Speeds," *Proc. ASME Turbo Expo*, 2017.

[4] J. L. Hee, R. Santhosh, K. Simmons, G. Johnson, D. Hann, and M. Walsh, "Oil Film Thickness Measurements on Surfaces Close to an Aero-Engine Ball Bearing Using Optical Techniques," *Proc. ASME Turbo Expo*, 2017.

[5] P. Gorse, K. Dullenkopf, H.-J. Bauer, and S. Wittig, "An Experimental Study on Droplet Generation in Bearing Chambers Caused by Roller Bearings," *Proc. ASME Turbo Expo*, no. 43147, pp. 1681–1692, 2008.

[6] A. A. Adeniyi, "A coupled Lagrangian-Eulerian framework to model droplet to film interaction with heat transfer," PhD Thesis, University of Nottingham, 2015.

[7] T. Pringuey, "Large Eddy Simulation of Primary Liquid-Sheet Breakup," PhD Thesis, Universtiy of Cambridge, 2012.

[8] J. Dick, V. Kumar, N. Pravin, and F. Montanari, "Simulation Of An Aero-Engine Bearing Compartment Using Two-Way Transition Between Lagrangian Droplets And A Three-Dimensional Eulerian Liquid Film," *Proc. ASME Turbo Expo*, 2019.

[9] M. Farrall, K. Simmons, and S. Hibberd, "A Numerical Model For Oil Film Flow in an Aero-Engine Bearing Chamber and Comparison with Experimental Data," *Proc. ASME Turbo Expo*, 2004.

[10] C. Wang, H. P. Morvan, S. Hibberd, and K. A. Cliffe, "Thin Film Modelling for Aero-Engine Bearing Chambers," *Proc. ASME Turbo Expo*, 2011.

[11] B. Kakimpa, H. Morvan, and S. Hibberd, "The Depth-Averaged Numerical Simulation of Laminar Thin-Film Flows With Capillary Waves," *J. Eng. Gas Turbines Power*, vol. 138, 2016.

[12] M. Farrall, S. Hibberd, and K. Simmons, "The Effect of Initial Injection Conditions on the Oil Droplet Motion in a Simplified Bearing Chamber," *J. Eng. Gas Turbines Power*, vol. 130, no. 1, pp. 1–7, 2008.

[13] B. Chen, G. D. Chen, H. C. Sun, and Y. H. Zhang, "Effect of oil droplet deformation on its deposited characteristics in an aeroengine bearing chamber," *Proc. Inst. Mech. Eng. Part G J. Aerosp. Eng.*, 2014.

[14] H. Sun, G. Chen, Y. Zhang, and L. Wang, "Theoretical and experimental studies on the motion and thermal states of oil droplet in a bearing chamber," *Proc. Inst. Mech. Eng. Part G J. Aerosp. Eng.*, 2016.

[15] Z. Jingyu, Z. X. Liu, J. P. Hu, and Y. Lu, "Numerical Modelling of Unsteady Oil Film Motion Characteristics in Bearing Chambers," *Int. J. Turbo Jet Engines*, vol. 32(3), pp. 233–245, 2015.

[16] P. Gorse, S. Busam, and K. Dullenkopf, "Influence of Operating Condition and Geometry on the Oil Film Thickness in Aeroengine Bearing Chambers," *J. Eng. Gas Turbines Power*, vol. 128, no. 1, pp. 103–110, Mar. 2004.

[17] Z. Jingyu and L. Zhenxia, "Numerical and experimental study for unsteady oil film thickness of the rotating cylinder chamber wall," *J. Eng. Gas Turbines Power*, vol. 137, no. 12, pp. 1–9, 2015.

[18] A. Nicoli, R. Jefferson-loveday, and K. Simmons, "A New OpenFOAM Solver Capable of Modelling Oil Jet-Breakup And Subsequent Film Formation For Bearing Chamber Applications," *Proc. ASME Turbo Expo*, pp. 1–12, 2019.

[19] A. A. Adeniyi, H. P. Morvan, and K. A. Simmons, "A Multiphase Computational Study of Oil-Air Flow Within the Bearing Sector of Aeroengines," *Proc. ASME Turbo Expo*, 2015.

[20] P. Gorse, K. Willenborg, S. Busam, J. Ebner, K. Dullenkopf, and S. Wittig, "3D-LDA Measurements in an Aero-Engine Bearing Chamber," *Proc. ASME Turbo Expo*, no. 36886, pp. 257–265, 2003.

[21] A. Bristot, K. Simmons, and M. Klingsporn, "Effect of Turbulence Damping in VOF Simulation of an Aero-Engine Bearing Chamber," *Proc. ASME Turbo Expo*, pp. 1–10, 2017.

[22] K. Singh, M. Sharabi, S. Ambrose, C. Eastwick, and R. Jefferson-loveday, "Prediction of Film Thickness of an Aero-Engine Bearing Chamber Using Coupled VOF and Thin Film Model," *Proc. ASME Turbo Expo*, 2019.

[23] A. B. Liu, D. Mather, and R. D. Reitz, "Modeling the effects of drop drag and breakup on fuel sprays," *SAE Tech. Pap.*, no. May, 1993.

[24] C. Bai and A. D. Gosman, "Mathematical Modelling of Wall Films Formed by Impinging Sprays," *SAE Trans.*, vol. 105, pp. 782–796, 1996.

[25] S. Mayer, "Theory of Liquid Atomization in High Velocity Gas Streams," *ARS J.*, vol. 31, pp. 467–473, 1961.

[26] M. A. Friedrich, H. Lan, J. L. Wegener, J. A. Drallmeier, and B. F. Armaly, "A separation criterion with experimental validation for shear-driven films in separated flows," *J. Fluids Eng. Trans. ASME*, 2008.

